Impact of carbon dioxide and nitrogen addition on the global structure of hydrogen flames

S. Eckart[1], G. Pio[2], T. Zirwes[3,4], F. Zhang[4], E. Salzano[2], H. Krause[1], H, Bockhorn[4]

Sven Eckart: sven.eckart@iwtt.tu-freiberg.de

[1]*Institute of Thermal Engineering, TU Bergakademie Freiberg, Freiberg, Germany*

[2]*Department of Civil, Chemical, Environmental and Materials Engineering, University of Bologna, Italy*

[3]*Steinbuch Centre for Computing, Karlsruhe Institute of Technology, Germany*

[4]*Engler-Bunte-Institute, Division of Combustion Technology, Karlsruhe Institute of Technology, Germany*

Abstract

Investigations into the combustion characteristics and flame structure of hydrogen/carbon dioxide/air flames have been carried out experimentally and numerically. The aim was to determine the variations of the combustion properties and flame shape for different carbon dioxide dilutions in the H_2-air mixtures. For this purpose, premixed flames at various compositions of hydrogen-carbon dioxide mixtures are investigated experimentally in a heat flux burner configuration at varying equivalence ratios from 0.5 to 1.1, fresh gas temperatures and under atmospheric conditions. Optical investigations are performed to detect the number of cellular structures on the flame front. Furthermore, the laminar burning velocity and the influence of carbon dioxide addition were examined numerically. A detailed kinetic mechanism was implemented for the identification of the most representative intermediates via a reaction path analysis, and the most influential species and reactions are identified through sensitivity analyses at conditions relevant to the studied application. Considering the nature of the adopted mechanism, the presence of CO_2 has the potential to shift the production/consumption rate of some hydrogen-containing radicals. Hence, numerical investigations employing an inert species having the same thermodynamic and transport properties as CO_2 (referred to as fictitious CO_2, FCO_2) were compared and discussed in this work. To investigate the effect of CO_2 on the dynamics of the hydrogen flames, one-dimensional and two-dimensional detailed simulations of the flame structure have been carried out. The addition of CO_2 makes the flame more prone to thermo-diffusive instabilities through a decrease in the mixture's thermal diffusivity. This results in a decrease of the Markstein number and an enhanced formation of characteristic cellular structures on spherically expanding flames. Overall, the comparison between the experimental and numerical investigations reveals similar conclusions.

Keywords: hydrogen admixtures, flame structure, CO_2, cellular structures

Introduction

To reduce CO_2 emissions, fossil fuels, such as natural gas, have to be replaced in the gas supply system by non-fossil energy carriers, such as hydrogen produced preferably from renewable sources. In this context, carbon oxides as by-products from hydrogen manufacturing are an increasingly important issue in the utilization of lower grade hydrogen. Technologies needed for the industrial utilization of hydrogen, e.g. safe transport and optimised combustion, are under rapid development or in the prototype stadium. Numerous industrial thermo-processes could run on gaseous mixtures rich in H_2 and CO_2, including hydrogen from biomass conversion, plastic waste treatment, thermal processes, steam reforming, and gasification processes [1]. Undoubtedly, new technologies based on H_2 for providing of energy (e.g., integrated gasification combined cycle or gas turbines) have been considerably improved in the last decades for reduction of air pollution. Commonly, a large variety of processed materials or operating conditions can be applied for these processes. For example, steam reforming and gasification can implement different charges (e.g., methane, naphtha, or coal) and have several target products (e.g., hydrogen, methanol, or ammonia), resulting in considerably different compositions of the product stream from the reactor (see Table 1, adapted from [2,3]).

These product streams usually are treated via several conversion and separation processes aiming at the reduction of impurities (e.g., sulphur-based species) and undesired by-products. Considering that 95 % of H_2 is produced via steam reforming worldwide [1], particular attention is paid to the conversion of CO when H_2 is manufactured for providing of energy. In this case, shift reactors are commonly integrated into the process to convert CO (Equation 1), with obvious implications on the H_2 to CO_2

volume ratio. Based on data reported in refs [1-4] for the ratio of H_2/CO for gasification processes, a proper amount of steam must be provided.

$$H_2O+CO \leftrightharpoons CO_2+H_2 \qquad (1)$$

Table 1 Typical composition of products gases from industrial processes delivering gaseous mixtures rich in H_2 and CO_2. Adapted from [2,3]

Process	H_2	CO	CO_2	CH_4	H_2O	H_2/CO_2	C/H
SR (Methane)	48.6	9.2	5.2	5.2	31.8	9,35	0.12
SR (Nafta)	34.6	5.3	8.0	8.0	44.1	4.33	0.14
MBG (Coal)	52.2	29.5	5.6	4.4	5.1	9.32	0.34
FBG (Coal)	27.7	54.6	4.7	5.8	4.4	5.89	1.01
EFG (Goal)	26.7	63.1	1.5	0.03	2.0	17.80	1.13

SR = Stream reforming, MBG = Moving Bed Gasifier, FBG = Fluidized Bed Gasifier, EFG = Entrained Flow Gasifier

Traditionally, a separation unit is employed to produce the H_2-rich stream for power generation and CO_2 for carbon sequestration. More recently, investigations have suggested the re-use of sequestered CO_2 as fracking agent [4]. Alternatively, the integration of water gas shift reactors and separation in a single unit has been intensively studied and referred to as sorption enhanced water gas shift (SEWGS) [5,6]. Dealing with highly pure H_2 streams raises concerns of safety during storage and transportation [7], and poses new challenges for environmental and technological aspects during combustion [8], e.g. production of pollutants such as NO_X [9]. On the other hand, the presence of CO_2 in the streams resulting from shift reactors offers alternative technological solutions utilizing its effects as a thermal diluent. Indeed, the use of CO_2 has been recently considered within the energy supply chain either as a service fluid for indirect heat transfer or as a component in the combustion chamber for direct heat transfer [10]. The latter approach includes the Allam’s Cycle [11] and it can be seen as an integrated strategy to recycle CO_2 from the carbon capture units, reducing the technical requirements. However, if traditional carbon-based fuels are considered, the presence of CO_2 alters the chemical equilibrium With these premises, direct combustion of H_2-CO_2 followed by carbon sequestration may be considered as a possible alternative, see Figure 1.

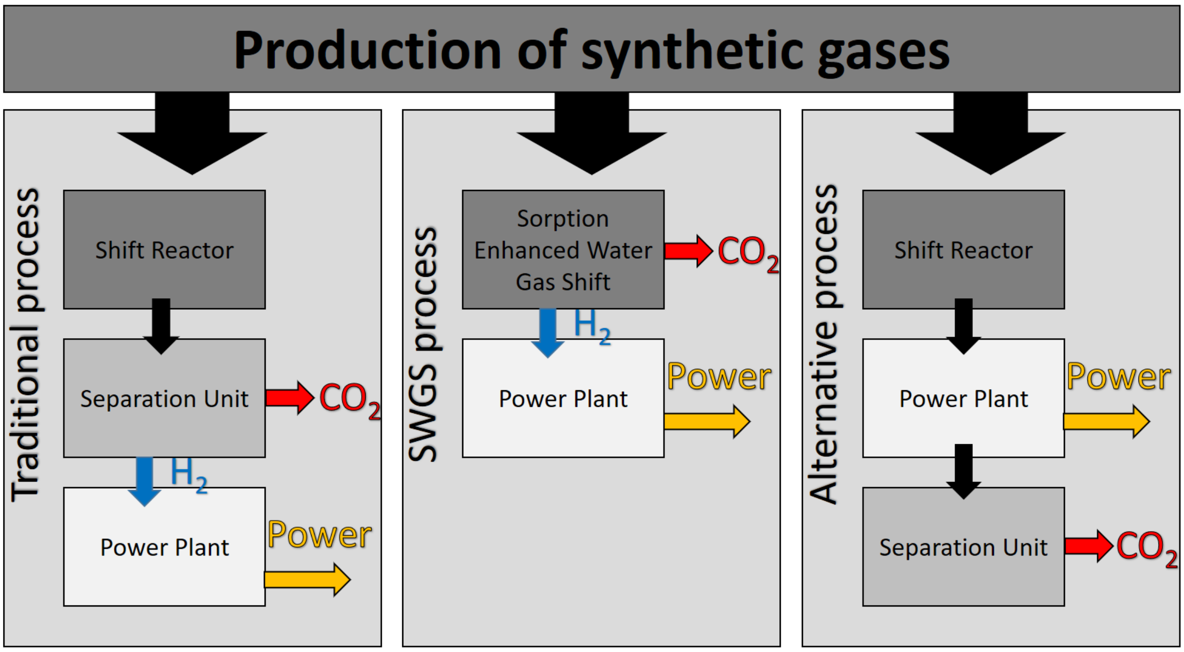

Figure 1 Schematic representation of synthetic gas-based processes

Quantitative investigations on the chemistry of combustion and flammability limits of H_2/CO_2-mixtures are missing at present. Indeed, most of the published studies dealing with the combustion chemistry of binary mixtures of C_0-C_1 species were devoted to the characterization of the interactions between CO and H_2 [12,13] in the view of synthetic gas utilization, or CH_4 and H_2 [14,15] for the application of hydrogen enriched methane flames [16]. The chemistry of H_2-CO_2 in complex mixtures was investigated as per the employment of oxygen-enriched air or pure oxygen [17] or in the case of biomass-derived fuels [18–21]. For safety relevant aspects, the effects of CO_2 addition on the hydrogen ignition limits were characterized by Djebaili et al. [22] at high temperatures, revealing the existence of non-thermal inhibition of the hydrogen oxidation.

The laminar burning velocities (LBV) of H_2/CO_2- mixtures were investigated at different temperatures and mixture compositions. For diluted H_2-air mixtures, planar flames formed in diverging channels could be used for the measurement. The effect of CO_2 is stronger than that of N_2 in reducing the burning velocity indicating a thermal and chemical effect of CO_2 dilution [23,24]. However, no apparent influence on the morphology of the planar flame due to the CO_2 admixture is reported. In other studies with flat flames, cellular structures were observed in CH_4, C_3H_8 and C_2H_6 flames [25] with high CO_2 dilution. Also, in flat flames stabilised on a McKenna burner, instabilities were observed in extremely lean CH_4-H_2-CO_2 flames with equivalence ratios of $\phi = 0.55$-0.69. Beyond that, no further studies on instabilities of the flame front due to the admixture of CO_2 are known [26]. The occurrence of cellular instabilities in adiabatic $H_2/O_2/N_2$ premixed flames anchored to a heat flux burner has been investigated numerically. Both hydrodynamic instabilities and diffusional instabilities leading to the formation of cellular flames were studied [27]. An adiabatic unstretched planar flame anchored to the heat-flux burner could only be realized within a critical lift-off distance. This lift-off distance seems to differ for each mixture. To explain the occurrence of these phenomena in more detail, insights from experimental and numerical investigations are necessary.

In this paper, H_2-CO_2-O_2-N_2 flames were investigated numerically to elucidate the effect of CO_2 dilution on combustion properties, flame structure and instabilities. The effects of CO_2 dilution on laminar burning velocity and Markstein length are investigated and quantified with 1-D simulation results using different reaction mechanisms. Further, the effects of CO_2-dilution on flame structure were investigated. Significant changes in flame morphology were found in experiments with H_2-CO_2-O_2-N_2 flames stabilized on a heat flux burner. The results were quantified as a function of plate temperature, unburned gas velocity and equivalence ratio. 2-D numerical simulations served to explain the appearance of the formation of cellular structures in the investigated flames.

1-D and 2-D Simulations, Numerical Setup and Procedure

Laminar burning velocity is generally considered a stand-alone parameter summarizing the interaction of convection, diffusion and chemical reactions during combustion [28]. In this work, the laminar burning velocity was estimated through the numerical simulation of one-dimensional, freely propagating, and adiabatic flames with the open-source software Cantera [29]. Absolute and relative tolerances for the steady-state problem were set to $1.0\cdot10^{-9}$ and $1.0\cdot10^{-4}$, respectively. Additional information about the numerical setup and adopted procedure can be found elsewhere [30].

A detailed kinetic mechanism composed of ~80 species and ~600 reactions, referred to as KiBO (Kinetics in Bologna) was employed because of the verified accuracy in reproducing the combustion chemistry of light species [28]. The initial temperature of T_{gas} = 298 K and atmospheric pressure were considered. Several combustible mixture compositions were tested, varying the equivalence ratio between ϕ = 0.5 - 6.0 and the H_2/diluent ratio by moles from 1.0 - 6.0. Either CO_2 or N_2 was used as diluent. The same conditions were used for fictitious CO_2 (i.e., FCO_2), as well. FCO_2 is an artificial species with the same thermodynamic and transport properties as CO_2, but not involved in any reaction.

A sensitivity analysis is performed by imposing a perturbation equal to 0.1 % of each input parameter (i.e., the rate constant of the *i*-th reaction, k_i) and evaluating the effects on the LBV (s_L). Results are expressed as normalized sensitivity coefficients (*NSC*), defined in Equation 2,

$$NSC = \left(\frac{k_{i,0}}{s_{L,0}}\right) \cdot \frac{\partial s_L}{\partial k_i} \qquad (2)$$

where the subscript 0 denotes the unperturbed values

Reaction path analysis identifies the key intermediates in the reaction path and quantifies the relative weight of each branch by estimating branching ratios. The relative width of the connection pathway is related to the relative contribution of the pathway to the species net yield [31]. In this work, a global pathway selection algorithm is implemented in a zero-dimensional constant volume system to identify the shortest paths connecting the most relevant species involved in the element flux. A threshold value of 0.01 is adopted for the selection of species to be included in the analysis. This approach allows for the generation of overall reaction paths. Hence, results are independent of the time instance, in contrast to the traditional path flux algorithm. Considering the analysed mixtures, the migration of H is investigated. Additional details of this methodology can be found in the references [32,33].

The effect of carbon dioxide dilution of hydrogen on possible thermo-diffusive instabilities is numerically investigated using one-dimensional and two-dimensional flames. In this context, the Markstein number Ma expresses how sensitive the burning velocity s_L, normalized by the flame speed of an unstretched flame $s_{L,0}$, is to the dimensionless flame stretch or Karlovitz number Ka:

$$Ma := -\frac{\partial s_L / s_{L,0}}{\partial Ka} \qquad\qquad Ka := \frac{1}{A}\frac{\mathrm{d}A}{\mathrm{d}t}\frac{d_{fl,0}}{s_{L,0}} \qquad (3)$$

where $d_{fl,0}$ is the thermal thickness of the unstreched flame front. A negative Markstein number is generally indicative of thermo-diffusively unstable flames. To quantify the Markstein number of hydrogen flames with different fuel dilutions, numerical simulations of counterflow-twin flames are performed with the open-source library Cantera [29]. In this axisymmetric setup, two opposed nozzles in 5 cm distance serve as inlets of the premixed hydrogen-diluent-air mixture at atmospheric conditions with a prescribed velocity. The oxidizer is air and the fuel is a mixture of hydrogen and the diluent. In all cases, the equivalence ratio is $\phi = 0.9$. The diffusion model is the mixture-averaged model applying the Hirschfelder-Curtiss approximation, thereby taking preferential diffusion into account.

Lastly, a detailed 2-D simulation of spherically expanding flames is conducted to study the evolution of cellular structures on the thermo-diffusively unstable flame during flame propagation.

Numerical results

Laminar Burning Velocity, Non-Stretched Flames

The effects of the CO_2 share in the unburnt mixture on the laminar burning velocity estimated at T_{gas} = 298 K and p_{gas} = 1 bar are reported in Figure 2 in dependence on the equivalence ratio. The case where N_2 was added to H_2 is included for comparison.

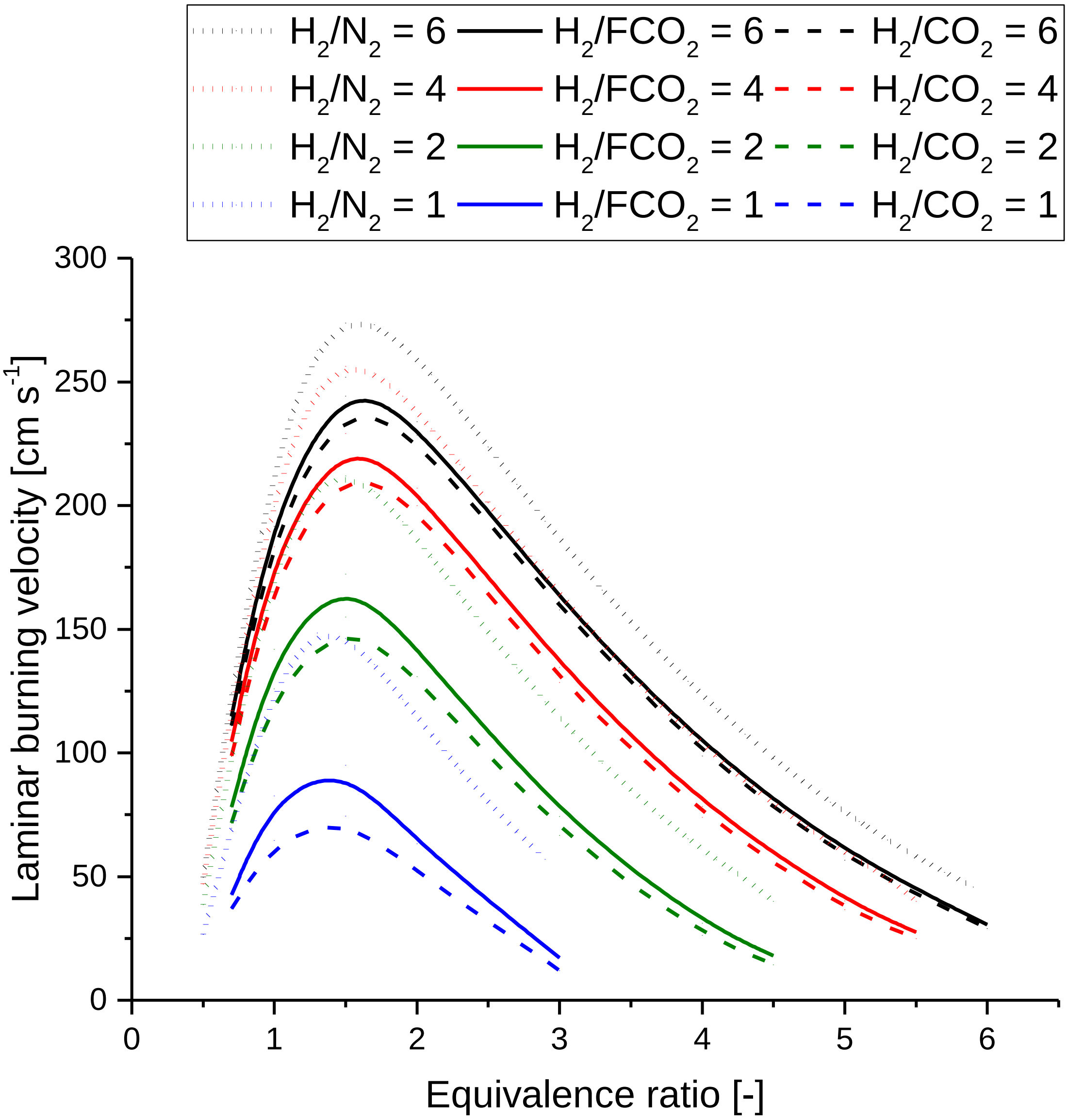

Figure 2 Comparison of estimated LBV at 298 K and 1 bar, in dependence on the equivalence ratio (the notation X/Y stands for the volume ratio).

The introduction of FCO_2 has a significant effect increasing the laminar burning velocity compared with CO_2 regardless of the H_2/CO_2 ratio, especially at near-stoichiometric compositions. The reduced overall burning velocity testifies to the chemical effects of CO_2. FCO_2 can be viewed as accounting for the thermal dilution only. The estimated laminar burning velocities of H_2/FCO_2 and H_2/N_2 mixtures show significantly larger values for the second case, regardless of the equivalence ratio and fuel composition considered. For example, the increase in the fundamental laminar burning velocity achieves values up to 50% for elevated dilution (i.e., low H_2/FCO_2 H_2/N_2 ratios). This trend can be explained considering the thermal inertia of the adopted diluents. It is worth noting that the observed increase in the laminar burning velocity can be linearly associated with the variation of the average heat capacity ($\bar{c_p}$), namely $LBV_{H_2/N_2}/LBV_{H_2/FCO_2} \approx \bar{c_p}_{H_2/N_2}/\bar{c_p}_{H_2/FCO_2}$. On the other hand, the magnitude of the effects of the chemistry of CO_2 on the LBV is largely influenced by the applied compositions. Indeed, the variation in the laminar burning velocity is limited to -10% for lean compositions, whereas it can reach ~-25% at stoichiometric and ~-40% in rich conditions. This trend is in line with the increased contribution of radicals in the conversion of the fuel typically attributed to the increase in equivalence ratios [34]. Considering the structure of the adopted mechanism, CO_2 plays either a direct role as a reactant/product dependent on the concentration or an indirect role as a diluent. The reaction associated with the formation of CO_2 via CO oxidation (i.e., $CO + OH \leftrightharpoons CO_2 + H$) is a clear example of the above-mentioned direct role. The presence of CO_2 alters the equilibrium, suppressing the formation of H radicals, thus potentially affecting the reactivity of the whole system. Conversely, reactions where CO_2 acts simply as inert diluent reducing the reaction rate by decreasing the reactant concentrations can be included into the group of indirect contributions.

For further clarification, the relevance of each reaction of the adopted mechanism was assessed through a sensitivity analysis. Although larger relative deviations between the dilution with FCO_2 and CO_2 are observed in rich compositions, the stoichiometric composition shows the largest absolute differences. Hence, the sensitivity analysis performed in this work was executed at 298 K, 1 bar, and stoichiometric composition (Figure 3) to assess the effect of CO_2 on the most influential reactions. For the sake of clarity, reactions are sorted by the absolute values of the NSCs and only the largest ten are listed.

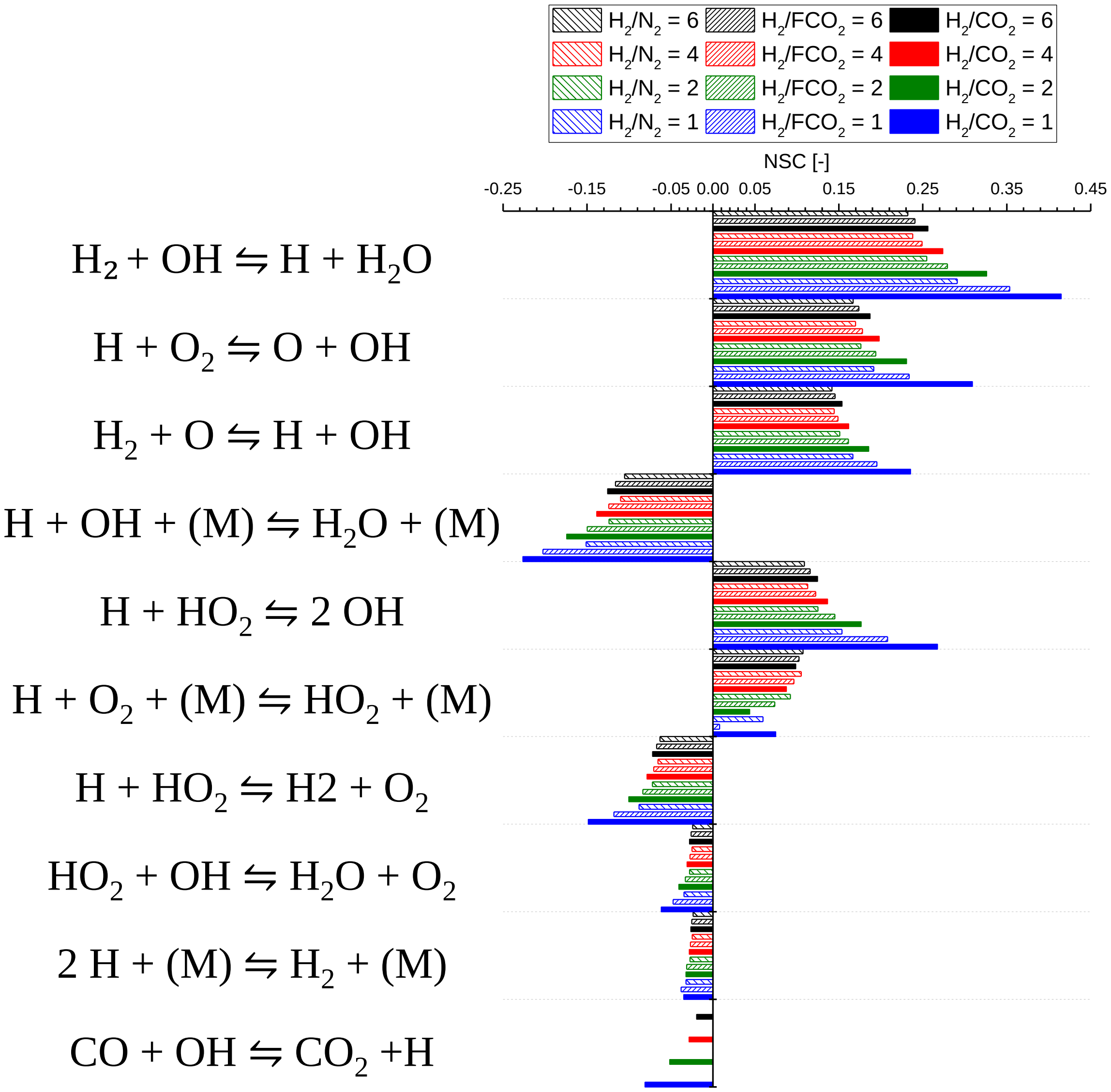

Figure 3 Comparison of normalized sensitivity coefficients of the laminar burning velocity with respect to the rate constants at 298 K and 1 bar, as a function of the initial fuel composition at stoichiometric conditions (the notation X/Y stands for the volume ratio).

Regardless of the chemical and thermal properties of the diluent, increasing the H_2 content leads to a general decrease in the absolute value of the NSCs. Besides, the comparison between the values for the FCO_2 and N_2 dilution shows slightly lower values for the latter case, except for the $H + O_2 + (M) \leftrightharpoons HO_2 + (M)$ reaction. This reaction represents the only case of a falloff reaction having CO_2 efficiencies lower than that of H_2 among the ones reported in Figure 3. This observation suggests that the competition between CO_2 (or FCO_2) and H_2 has a detrimental effect on $H + O_2 + (M) \leftrightharpoons HO_2 + (M)$.

Conversely, the direct role of CO_2 can be evaluated through the comparison between the CO_2 and FCO_2 data. In most cases, larger NSCs are calculated for CO_2 dilution for a given fuel composition. These trends imply that the presence of CO_2 makes the systems more sensitive to the chemistry of OH and H radicals either from a kinetic or thermal point of view. It should be noted that the most influential reaction directly involving CO_2 is $CO + OH \leftrightharpoons CO_2 + H$. NSCs corresponding to the FCO_2 and N_2 cases are negligible for this reaction due to the inert character of these reactants. Hence, the presence of CO_2 can promote the formation of CO and OH through the reverse reaction consuming H. Besides, this reaction offers the possibility to explain the differences in laminar burning velocities, as the NSC is negative and the reaction is typical of near stoichiometric mixtures. These observations can be confirmed by the reaction path analysis shown in Figure 4 for equimolar fuels (i.e., H_2/CO_2 and H_2/FCO_2 equal to 1) under flame conditions, namely 1200 K, 1 bar, and stoichiometric mixture composition.

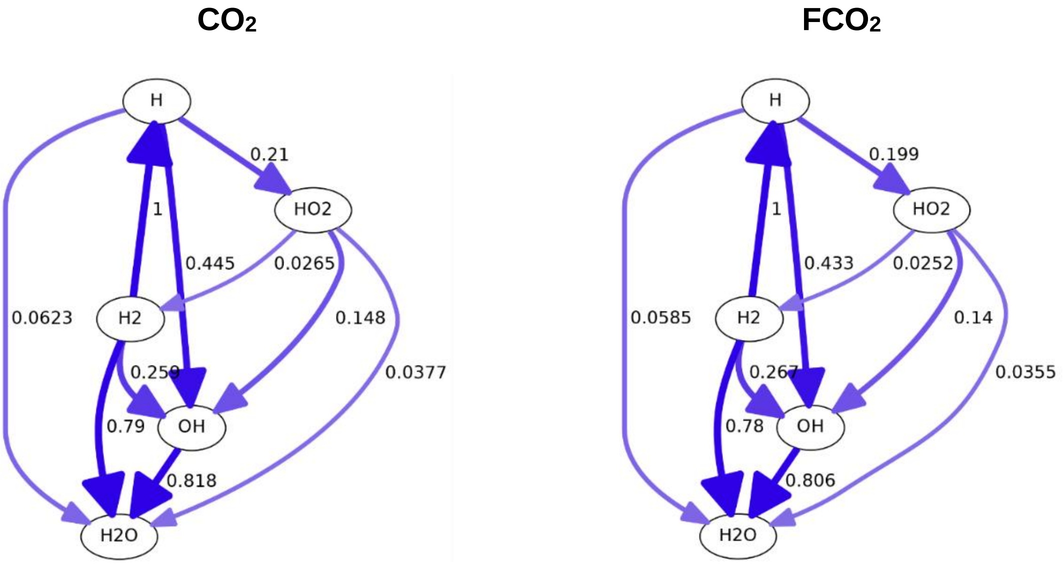

Figure 4. Reaction path analysis for CO_2 and FCO_2 in equimolar composition with H_2 and stoichiometric conditions at initial temperature 1200 K and 1 bar.

Although the general structure of the presented reaction paths is not affected by the fuel composition, significant variations in branching ratios can be observed. The flux diagrams indicate that the presence of CO_2 slightly affects the relative contribution of branches producing small radicals, except for the direct production of H. Looking at the intermediates resulting from primary reactions involving H_2, OH is favored by FCO_2 to the detriment of direct H_2O formation. Combining these observations with the results of the sensitivity analysis, it is obvious that CO_2 affects the competition between $H_2 + O \leftrightharpoons H + OH$ and $H_2 + O$

+ (M) ⇋ H_2O + (M). It should be noted that CO_2 and FCO_2 have the same collision efficiencies for any third body reaction included in the mechanism, leaving the reaction rate of H_2 + O + (M) ⇋ H_2O + (M) unaffected. Therefore, the abovementioned differences can be mainly attributed to the difference in temperature due to the modified global heat release of the systems. The resulting excess in OH suppresses its production from H and HO_2, mostly attributable to H + HO_2 ⇋ 2 OH. Following the observations derived from the sensitivity analysis, the branch connecting H to OH is diminished by about 3% at the investigated conditions through FCO_2 with the chemical contribution from CO + OH ⇋ CO_2 + H.

Laminar Burning Velocity, Stretched Flames

To investigate the effect of CO_2 dilution on the burning velocity of stretched flames and possibly flame instabilities a one-dimensional counterflow-twin flame is considered. The setup consists of two opposed nozzles with identical premixed hydrogen-diluent-air mixtures at atmospheric conditions. Three cases at $\phi = 0.9$ are considered, where the fuel consists of a) pure hydrogen, b) 30 mol-% hydrogen and 70 mol-% CO_2, and c) 30 mol-% hydrogen and 70 mol-% nitrogen. All cases are computed using the DRM19 reaction mechanism [35], which has been used in the literature for similar conditions, and the KiBO mechanism. Figure 5 shows the burning velocity over Karlovitz number, which represents the non-dimensional flame stretch (see equation 3) for the different fuel mixtures. The flame with pure hydrogen as a fuel has a positive Markstein number, which is indicative of a thermo-diffusively stable flame. The flame with nitrogen dilution has a Markstein number close to zero and is therefore insensitive to flame stretch. The flame with CO_2 dilution on the other hand has a negative Markstein number.

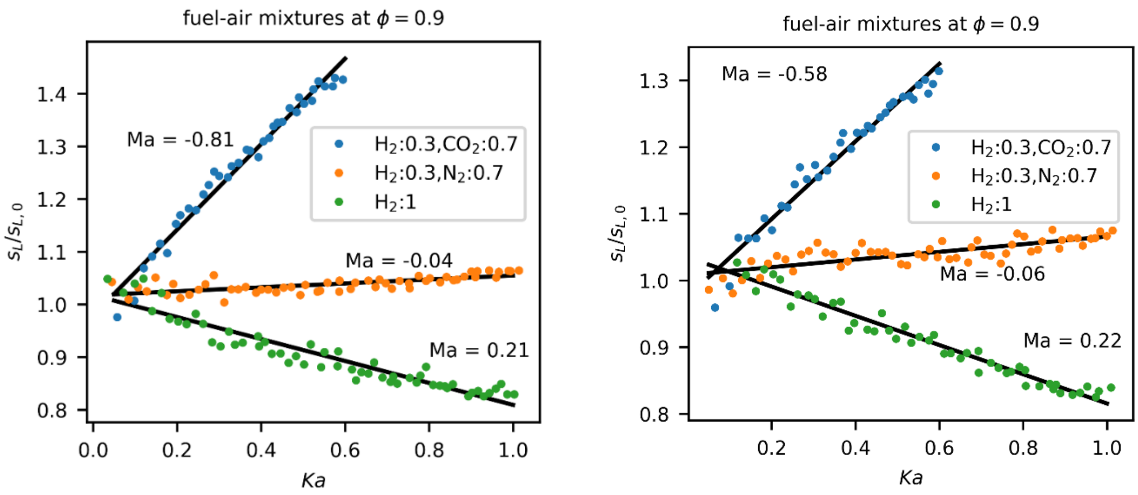

Figure 5 Burning velocity over Karlovitz number from the counterflow-twin flames for different fuel mixtures and resulting Markstein numbers. Left: DRM19 reaction mechanism. Right: KiBO reaction mechanism.

The negative Markstein number resulting from the CO_2 dilution is mainly attributed to the reduction of the thermal diffusivity of the gas mixture and therewith the reduction of the Lewis number. The thermal diffusivity of the fuel-oxidizer mixture with pure hydrogen at $\phi = 0.9$ is $a = 4.5 \times 10^{-5}$ m²/s, while the mixture thermal diffusivity with CO_2 dilution is $a = 2.9 \times 10^{-5}$ m²/s. The simulation with CO_2 dilution has been repeated by replacing CO_2 with the chemically inert FCO_2. Disabling the conversion of CO_2 leads to slightly higher burning velocities and a slightly larger Markstein number ($Ma = -1.0$), but otherwise the same trend is found. Likewise, changing the diffusion model from the mixture-averaged model to the multi-component model including the Soret effect yields a similar Markstein number of -0.99 for the H_2-CO_2 mixture and +0.21 for the pure hydrogen flame (compare with Tab. 2). Several strategies for the development of detailed kinetic mechanisms can be used, including manual enlargement or automatic generation [36]. The selected strategy as well as the approach to compute thermodynamic and kinetic data to be used as input, strongly affect the laminar burning velocity predicted by the produced mechanisms, as recently demonstrated [37]. Nevertheless, the identification of the most accurate model for the hydrogen case is still a challenging task. Indeed, a comparison of the experimental measurements for the laminar burning velocity of hydrogen-containing mixtures from different setups shows a significant variability of this parameter [38]. On the other hand, the comparison of estimated laminar burning velocity obtained by different mechanisms can provide useful information on the robustness and validity of physical models.

To validate these results, simulations of cases a) and b) have been repeated with the detailed GRI 3.0 reaction mechanism [39] and the reduced reaction mechanism by Kee [40]. For the pure hydrogen flame, the reaction mechanisms by Li et al. [41], Konnov [42], and Connaire et al. [43] were included in the comparison as well. While there are slight differences in the predicted burning velocity and Markstein number, they all show the same tendency, i.e. a change from a flame with $Ma > 0$ for pure hydrogen as fuel to a flame with $Ma < 0$ when considering dilution with CO_2. The results are summarized in Table 2. Flames with $Ma < 0$ are potentially thermo-diffusively unstable. All predictions can be included within the uncertainty range typically associated with laminar burning velocity measurements [44]. It should be noted that the GRI3.0 reaction mechanism has not been originally validated for methane-CO_2 blends and thus shows considerable differences in flame speed compared with other reaction mechanisms, especially for case b. The tendency of GRI3.0 to underestimate the overall reactivity has been already reported for low-carbon fuels [45]. Nonetheless, GRI3.0 is still widely used today. Even though the prediction of the laminar flame speed differs, the observed trend of CO_2 addition stays the same: the Markstein number of the reactive mixture changes from positive to negative, showing that the addition of CO_2 leads to a potentially thermos-diffusively unstable flame.

Table 2 Burning velocity and Markstein number from the counterflow-twin flames obtained with different reaction mechanisms at ϕ = 0.9

Case a (100 mol-% H_2)

Mechanism	$s_{L,0}$ (m/s)	Ma
DRM19	2.24	+0.21
KiBO	2.12	+0.22
GRI3.0	2.02	+0.33
Kee	2.21	+0.32
Li	2.02	+0.30
Konnov	2.03	+0.33
Connaire	1.97	+0.28

Case b (30 mol-% H_2, 70 mol-% CO_2)

Mechanism	$s_{L,0}$ (m/s)	Ma
DRM19	0.111	-0.81
KiBO	0.107	-0.58
GRI3.0	0.066	-1.07
Kee	0.138	-0.74

Experiments for determining of the flame front instabilities

As stated above, flames with $Ma < 0$ are potentially thermo-diffusively unstable. To investigate thermo-diffusive instabilities and non-stable flame fronts, a flat flame burner with a stabilized flame was selected also allowing optical examination of changes in the flame front over long examination intervals. These burners are usually used to determine the laminar burning velocity of quasi-adiabatic flat flames. The heat flux burner design used in the present work was proposed by de Goey et al. [46], based on the fundamental experimental work done by [47]. The method has the advantage of directly measuring the LBV of a planar stationary unstretched flame. The stabilization of a planar flame has been further proved by [48] and can be achieved with a temperature-controlled burner plate compensating heat losses from the flame. In the experimental setup used here the gas flow is controlled by three calibrated mass flow controllers (MFCs). The ambient conditions as well as the signals from newly integrated type T thermocouples are recorded and used to calculate the LBV [49]. By definition, the determination of the laminar burning velocity is only possible for planar flames. Therefore, the radial temperature profiles of the plate are fitted ba parabolic functions and analysed for up to 350 measurements to find conditions for adiabatic stabilisation of the flame, i.e. the parabolic coefficent C of the radial temperature profile equals 0, see middle of figure 6. For further details of the setup [50,51] and experimental uncertainties [52] related to gas flows and other possible sources of errors, refer to Eckart et al. [53–56] and Rau et al. [57]. If instabilities and cellular structures occur, a determination of the LBV is not permissible.

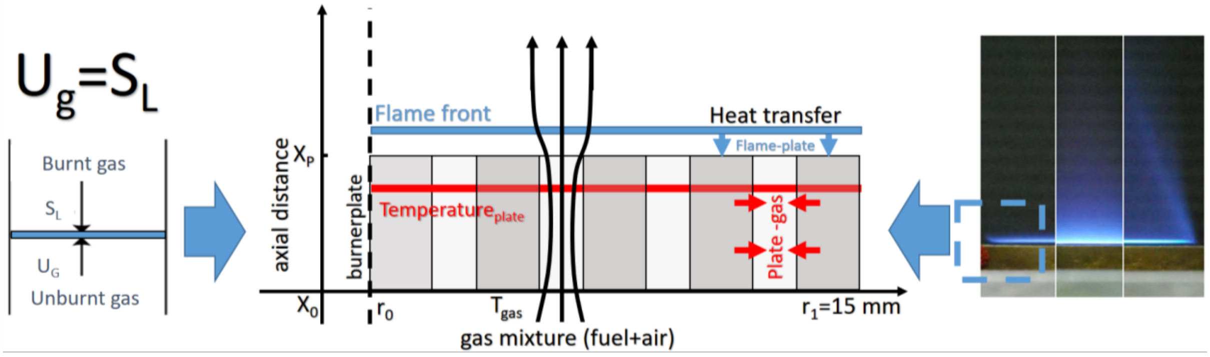

Figure 6 Schematic drawing of the heat flux burner setup and the position of the stabilized flame.

Experiments are conducted at equivalence ratios (ϕ = 0.5–1.1) and CO_2 contents up to 70% in hydrogen. The initial gas temperatures are 300 K. Under these conditions, cellular structures could be observed. To evaluate the behaviour of the flames and their instabilities, a VIS-camera was mounted above the heat flux burner. With this optical setup, 10 pictures of the stabilized flame were taken at a time interval of 120 s. These pictures were then evaluated carrying out a step binarization and reduction of small interference effects due to reflections. Subsequently, edge detection and a watershed transformation were performed in a parameterized manner. This procedure made it possible to separate flame structures from each other. The number of separated flames was evaluated and displayed graphically as an overlay. The procedure can be seen systematically in Figure 7.

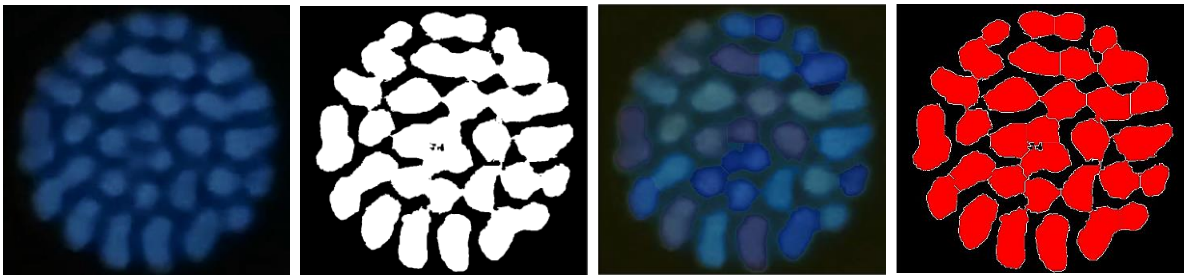

a) b) c) d)

Figure 7 Steps of image processing, a) raw data of the heat flux flame, b) binarization and reduction of reflections, and c) overlay of cells detected by watersheded transformation and d) counting.

Experimental results for flame structures

Experimental results obtained at atmospheric pressure for hydrogen-carbon dioxide-air mixtures at various equivalence ratios of ϕ = 0.5 - 1.1 were analyzed. Figure 8 shows the comparison of measured unburnt gas velocity and the parabolic coefficient C for equivalence ratio ϕ = 0.9 and a flame with 30 mol-% hydrogen diluted by 70 mol-% of CO_2. In the experiments, different plate temperatures (368-428 K) were applied. It was observed that the plate temperatures affect the parabolic coefficient, which is normally used to interpolate to the adiabatic state. The plate temperature did not influence the overall trend of the results. Since all the flames were not planar and therefore did not correspond to the theoretical prerequisites for the determination of the laminar burning velocity, the inflow velocity cannot be considered the same as the burning velocity even if the parabolic coefficient is $C = 0$. The determination of the laminar adiabatic curvature and stretch free burning velocity was not possible for the investigated regions, as impairments were detected in the flame in all cases. In the experiments, it could be shown that with an increase in the velocity at the outlet and a corresponding increase in the volumetric flow rate, the temperature in the middle of the plate decreased in the order of $\Delta T_{max} \approx 15$K. These changes also had no influence on the flame shape of the H_2-CO_2-O_2-N_2 flames.

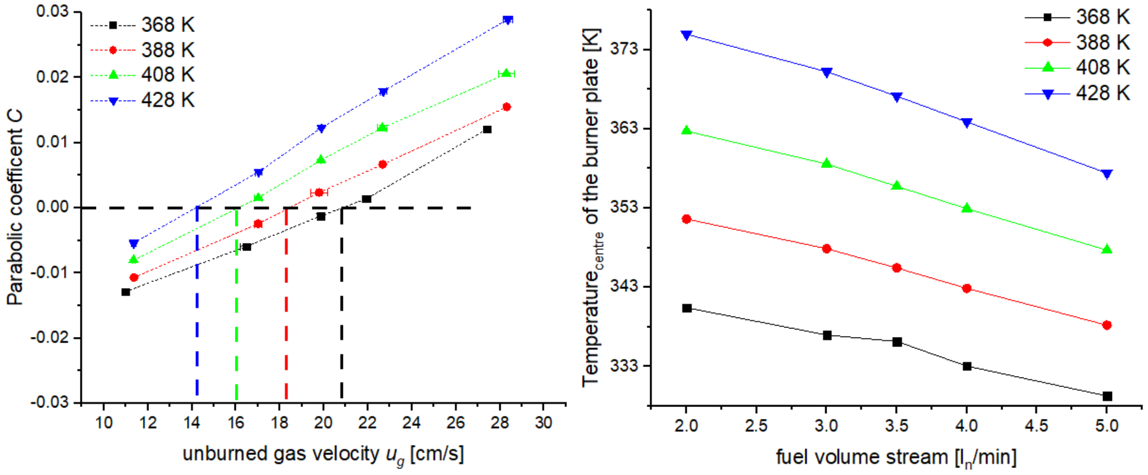

Figure 8 Measured parabolic coefficient and fuel volume stream as a function of plate temperature for a flame with 30 mol-% H_2 diluted by 70 mol-% of CO_2, for equivalence ratio ϕ = 0.9 and T_{gas} =300 K

In Figure 9 the flame morphology with view from above and from the side at the plate temperature of T_{plate} = 368 K and varying flow rates are illustrated. The flames have been operated with 30 mol-% hydrogen diluted by 70 mol-% of CO_2 at an equivalence ratio ϕ = 0.9 and T_{gas} = 300 K. It can be seen that the intensity of the individual flame structures increases significantly with inflow velocity. With increasing inflow velocity, the flames are also stabilized further away from the burner plate and a "sealed" flame front is no longer appearing. The change of this state can be seen in the range from 3 to 4 l_n/min, whereby the transition from negative to positive parabolic coefficients can also be detected (see Figure 8).

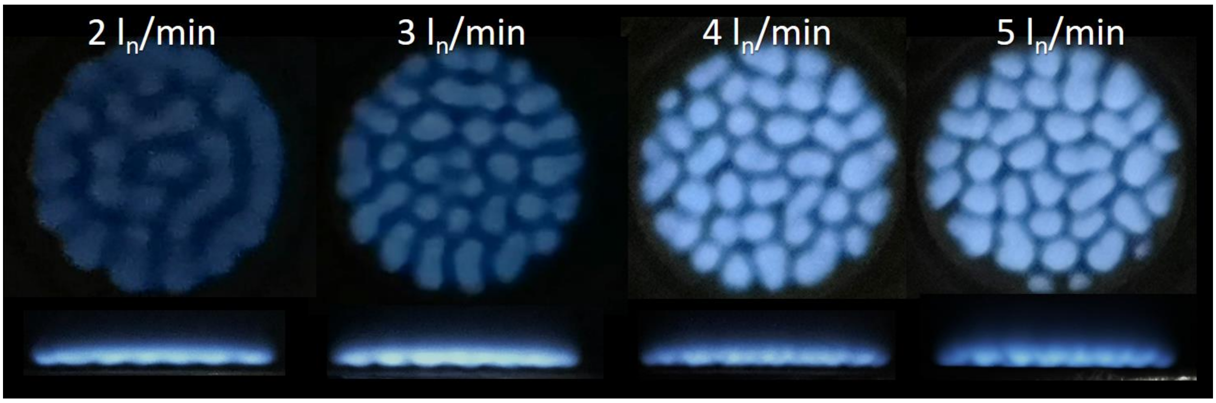

Figure 9 Flame morphology for different volume streams with 30 mol-% hydrogen and 70 mol-% carbon dioxide for an equivalence ratio of ϕ = 0.9, T_{gas} = 300 K and T_{plate} = 368 K, top: top view, bottom: side view

For two different image series, one depending on the fuel flow rate and one on the equivalence ratio, the number of cells in the broken flame front was analysed. The series were recorded independently of each other. However, it can be seen that both overlap ~~in~~ within the uncertainty~~ies~~ regions. The maximum number of cells is again located in the range of parabolic coefficients around *C* = 0. The number of cells is in the same order of magnitude as found by Konnov et al. for methane flames, but below the ones of ethane and propane flames. In this study, however, "closed" flame fronts were frequently found [25]. For the highest volume flow rate tested, an evaluation of the number of individual cellular flames as a function of the equivalence ratio was carried out according to the procedure described above. It turns out that a maximum of around 45 cells could be found, as seen in Figure 10 b). Konnov et al. [25] could find the maximum cell count for methane flames in the range of ϕ = 0.8, whereas for ethane and propane higher values were observed at ϕ = 1.2-1.4 and 1.3, respectively.

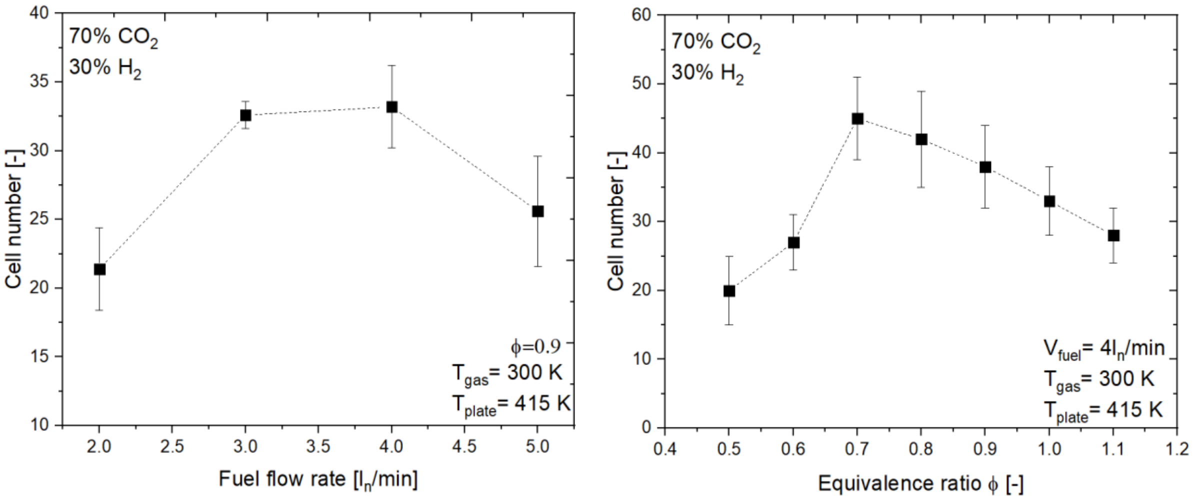

a)

b)

Figure 10 Cell number a) depending on the fuel flow rate and b) the equivalence ratio

2-D Numerical Simulation of Spherically Expanding Flames

To investigate the thermo-diffusive instabilities caused by the CO_2 dilution further and to assess the structure of the flames, detailed simulations of spherically expanding, constant pressure flames in initially quiescent premixed fuel-air mixtures at atmospheric conditions ($p = 1\ \mathrm{atm}, T = 300\ \mathrm{K}$) are conducted. A H_2-air (case a**,** $\phi = 0.9$, 100 % H_2) and a H_2/CO_2-air flame from case b ($\phi = 0.9$, 30 mol-% H_2 and 70 mol-% CO_2) are simulated. The computational setup consists of a quasi-3D domain, which is a wedge-shaped half-sphere, as shown in Figure 11. For the flame of case a, the diameter of the computational domain is 16 cm and the mesh consists of 8.1 million finite volumes, yielding a resolution in the equidistant region of the mesh of 33 µm. For the CO_2 diluted flame of case b, the diameter of the domain is 48 cm and consists of 65 million finite volumes with a resolution of 56 µm. The finer mesh for the flame in case a is required due to the pure hydrogen flame having a lower flame thickness. Similarly, the flame speed of the CO_2 diluted flame is lower, and therefore a larger propagation distance is required for the flame to develop the thermo-diffusive instabilities. In both cases, the flame zone is fully resolved with more than 15 cells.

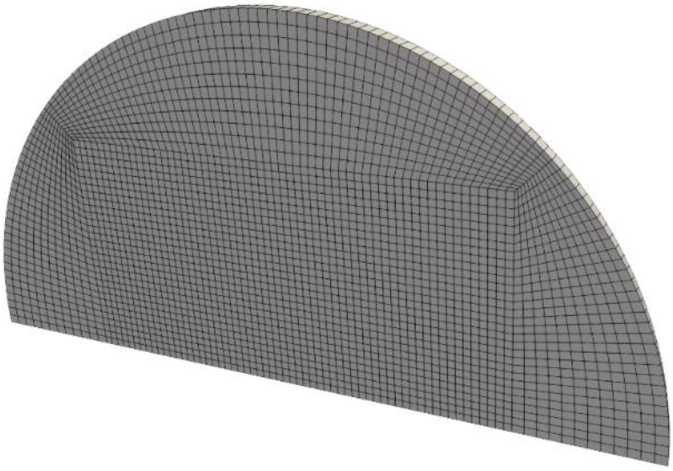

Figure 11 Computational domain for the spherically expanding flames

The simulation is performed with an in-house solver for the detailed simulation of flames [58–60] based on OpenFOAM [61] and Cantera, which has been validated in previous works [62–65]. It solves the fully compressible Navier-Stokes equations together with a balance equation for energy and each chemical species. The conservation of total mass reads

$$\frac{\partial \rho}{\partial t} + \nabla \cdot (\rho \vec{u}) = 0 \tag{4}$$

ρ is the density, t time and $\vec{u}$ is the gas velocity. The conservation of momentum is expressed as

$$\frac{\partial (\rho \vec{u})}{\partial t} + \nabla \cdot (\rho \vec{u} \vec{u}) = -\nabla p + \nabla \cdot \tau \tag{5}$$

with p the pressure and τ the stress tensor

$$\boldsymbol{\tau} = \mu \left(\nabla \vec{u} + \nabla \vec{u}^{\mathrm{T}} - \frac{2}{3} \nabla \cdot \vec{u} \boldsymbol{I} \right) \tag{6}$$

and μ being the dynamic viscosity of the reacting mixture. $\boldsymbol{I}$ is the unit tensor. The balan~~an~~ce of species masses is expressed in terms of the mass fractions Y_k of species *k*

$$\frac{\partial (\rho Y_k)}{\partial t} + \nabla \cdot (\rho \vec{u} Y_k) = \dot{\omega}_k - \nabla \cdot \vec{j}_k \tag{7}$$

where $\dot{\omega}_k$ is the reaction rate of species *k* and $\vec{j}_k$ its diffusive flux. Species diffusion is computed from a mixture-averaged approach

$$\vec{j}_k = -\rho D_k \nabla Y_k \tag{8}$$

where D_k is the diffusion coefficient of species k computed from kinetic gas theory. The energy balance is formulated in terms of the total sensible enthalpy:

$$\frac{\partial(\rho(h_s + \frac{1}{2}\vec{u} \cdot \vec{u}))}{\partial t} + \nabla \cdot (\rho\vec{u}(h_s + \frac{1}{2}\vec{u} \cdot \vec{u})) = -\nabla \cdot \vec{q} + \frac{\partial p}{\partial t} - \sum_k h_k^\circ \dot{\omega}_k \tag{9}$$

h_k° is the enthalpy of formation of species k and h_s the sensible enthalpy of the mixture. $\vec{q}$ is the diffusive heat flux

$$-\nabla \cdot \vec{q} = \nabla \cdot \lambda \nabla T - \sum_k \nabla \cdot h_{s,k} \vec{j}_k \tag{10}$$

where λ is the heat conductivity of the gas mixture, T ist the temperature and $h_{s,k}$ the sensible enthalpy of species k.

The DRM19 reaction mechanism is used and chemical reaction rates are computed from finite rate chemistry. The diffusion model is the mixture-averaged model. For time discretization, a second order implicit method is used, while spatial discretization is based on fourth-order interpolation schemes. The initial condition is given by a spherical flame kernel with a radius of 2 cm, obtained from a one-dimensional pre-cursor simulation of a spherically expanding flame. The subsequent flame propagation and development of instabilities is then captured during the simulation in detail.

Figure 12 shows the temporal evolution of the flame front for the hydrogen-CO_2 fuel mixture of case b during flame propagation in terms of the heat release rate (HRR) at different time instances. The flame starts from a perfectly spherical configuration. While the flame expands, cellular structures form on the flame front. The red box indicated in the top figure is later discussed in Figure 14.

At negatively curved parts of the flame front, the flame locally extinguishes, which is consistent with the negative Markstein number. The structure of the cell formation follows the typical flame finger configuration [66]. In this way, the H_2-CO_2 flame at $\phi = 0.9$ behaves the same as thermo-diffusively unstable, lean ($\phi \ll 1$) pure hydrogen flames [67].

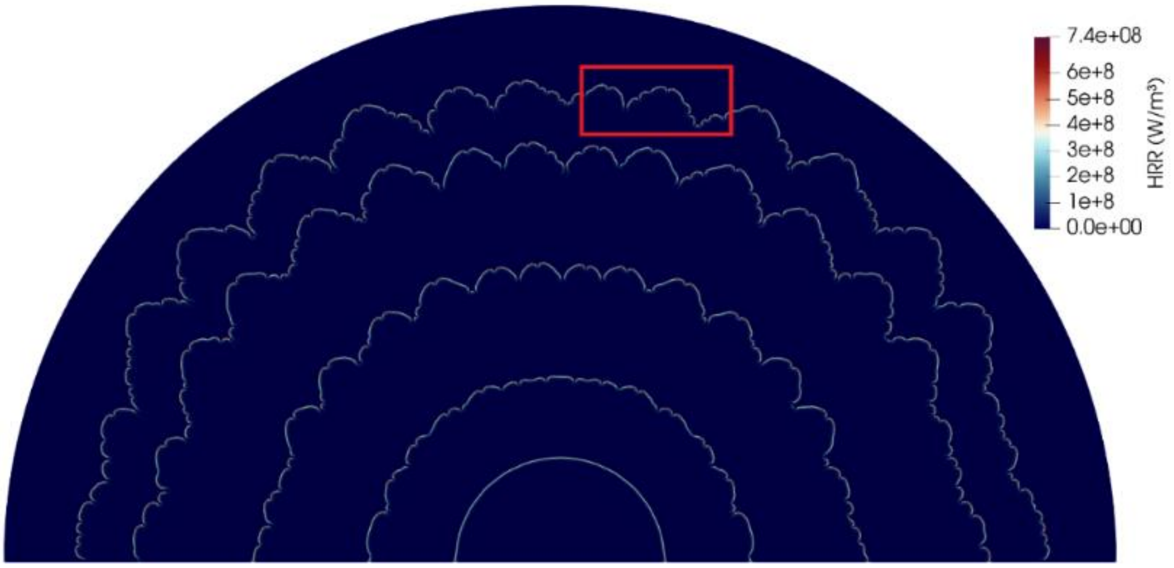

Figure 12 Flame front indicated by the heat release rate (HRR) at different time instances for the flame from case b during spherical propagation.

Figure 13 shows the propagating pure hydrogen flame at $\phi = 0.9$, again in terms of heat release rate at different time instances. As the flame reaches a sufficient radius, it becomes corrugated. However, this corrugation is not an effect of thermo-diffusively unstable cellular structures, but a hydrodynamic instability due to thermal expansion across the flame front (Darrieus-Landau instability), lacking the typical structure of the flame fingers or thermo-diffusive cells. This distinction is shown in Fig.14.

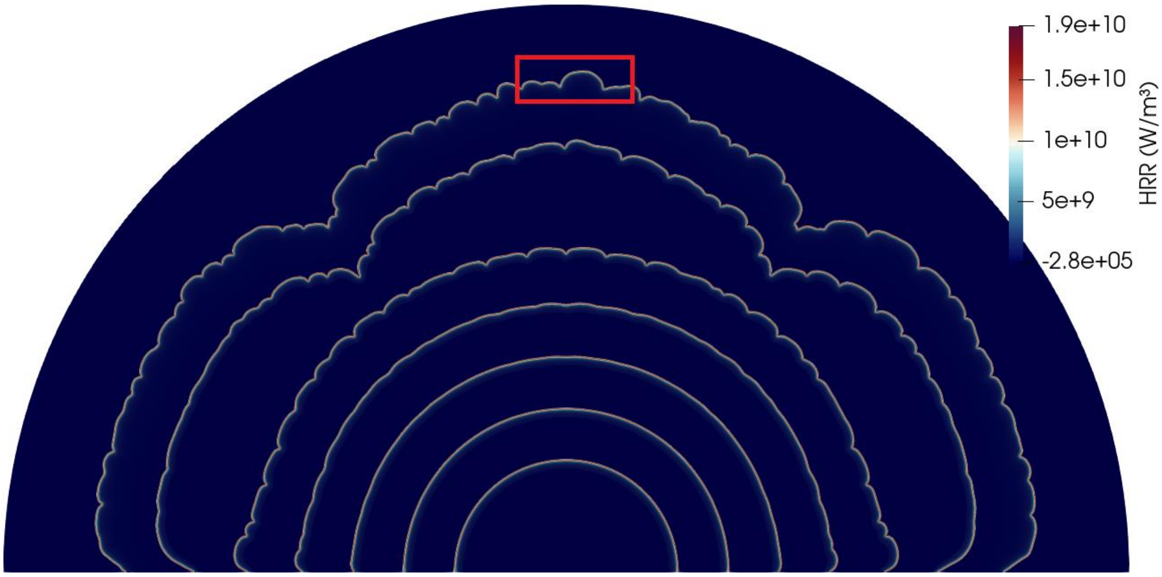

Figure 13 Flame front indicated by the heat release rate (HRR) at different time instances for the flame from case a during spherical propagation.

The reaction zones indicated by the red boxes from Fig. 12 and 13 are zoomed-in in Fig. 14. The top figure shows the CO_2 diluted flame. Due to the cellular structures caused by the thermo-diffusive instability, characteristic flame fingers develop [66]. These also have a characteristic length scale, in this case with a diameter of about 3 cm. The depicted heat release rate field also shows that the flame locally extinguishes at the negative curved parts of the flame front, and locally enhances at the positively curved parts of the flame front. This is in accordance with the negative Markstein number, as computed from the one-dimensional counterflow flame simulations. In this way, the H_2-CO_2 flame at $\phi = 0.9$ behaves the same as thermo-diffusively unstable, lean ($\phi \ll 1$) pure hydrogen flames [67].

On the other hand, the zoom into the flame front of the pure hydrogen flame at $\phi = 0.9$ does not show the typical cellular structure of thermo-diffusively unstable flames. Instead, the corrugations on the flame front are irregular, eventually forming cusps consistent with hydrodynamic instabilities. Again, in accordance with the low positive Markstein number from Table 2, the correlation of local heat release rate and flame curvature is reversed: in this case, the local heat release rate becomes maximal at the negatively curved parts of the flame front. Since the Markstein number is close to zero, the sensitivity of local flame speed or heat release rate with respect to flame curvature is low. Therefore, the variation of HRR along the flame front is low and no local extinction occurs.

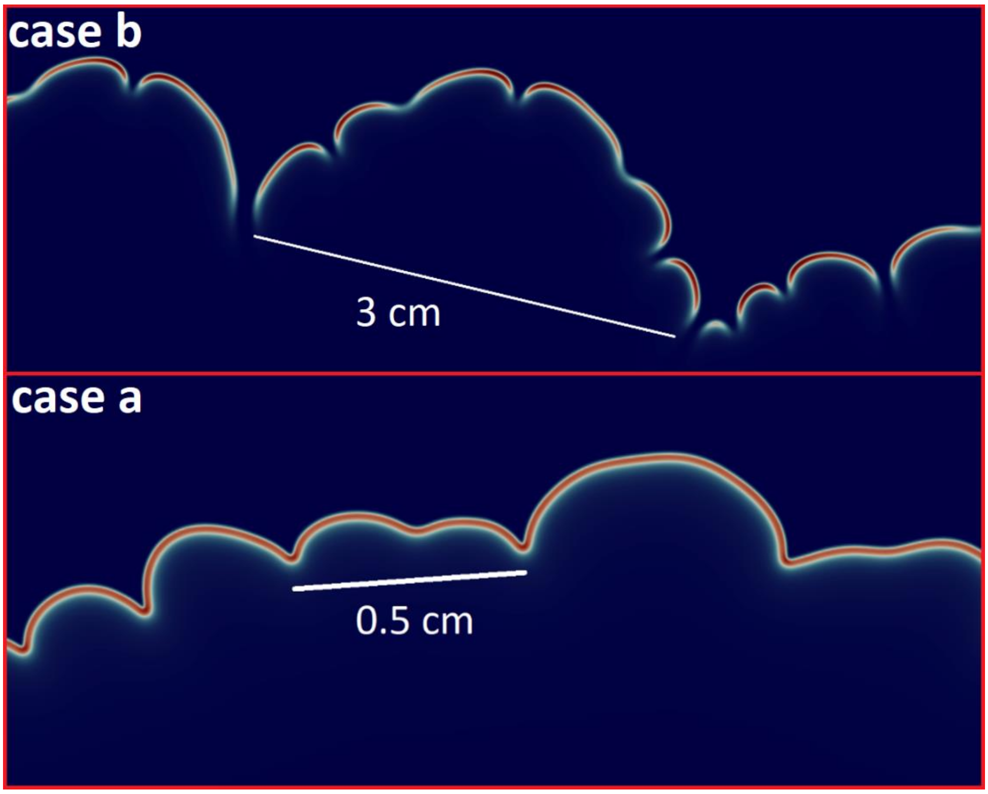

Figure 14 Zoomed-in regions from Fig. 12 and 13. Top: heat release rate field from the CO_2 diluted flame from case *b*, showing the regular structure of the thermo-diffusively unstable cells. Bottom: heat release rate field from the pure H_2 flame from case *a*, where the corrugation results from a hydrodynamic instability with little variation of heat release rate along the flame front.

Conclusions

In this paper premixed H_2-CO_2-O_2-N_2 flames with air were investigated first numerically and the findings have been afterwards confirmed in an experimental investigation. The utilization of a validated detailed kinetic mechanism allowed for the evaluation of the effects of initial composition on the laminar burning velocity, the most influential reactions, and the main oxidation paths of the investigated mixtures. The relative contribution of thermal and chemical effects was quantified through the definition of a fictitious CO_2 (FCO_2), acting as an inert species having the same thermal and transport properties as CO_2. The obtained results showed that the presence of CO_2 strongly affects the chemistry of non-carbon containing species because of the modifications in the reaction rate of $CO + OH \leftrightharpoons CO_2 + H$, potentially causing significant differences in the ignition behavior. Further, the effect of CO_2 addition in terms of the flame structure has been investigated with two different numerical setups: the addition of CO_2 leads to a decrease in the mixture's thermal diffusivity and therewith a decrease in the Lewis number. This in turn changes the Markstein number for near-stoichiometric flames from slightly positive values for pure hydrogen flames to negative ones for H_2-CO_2 flames. These results are independent of the employed reaction mechanisms and also if CO_2 is considered an inert species or not. Detailed simulation of a spherically expanding H_2-CO_2 flame shows the expected cellular structures of thermo-diffusively unstable flames, which is not present for the pure hydrogen flame.

These results were verified by experiments using a heat flux burner. Adiabatic cellular flames of H_2-CO_2-O_2-N_2 were identified visually and by photographic observations and the cellular structures have been quantified. Under specific experimental conditions, the flames become cellular; this led to significant modification of the flame propagation speed. Increasing the temperature of the burner plate up to T_{plate} = 428 K does not eliminate this instability for H_2-CO_2-O_2-N_2 flames. Lowering the temperature of the burner plate extended the range of equivalence ratios over which cellularity was observed. No direct proportionality between the number of cells and inlet velocity in H_2-CO_2-O_2-N_2 flames was observed. Dependence of the number of cells as a function of equivalence ratio clearly showed a local maximum in the lean mixtures. In future studies, the influence of CO_2/H_2 ratios as well as the influence of pressure and temperature on these instability phenomena will be investigated in more depth.

Acknowledgments

The work leading to this publication was supported by the PRIME program of the German Academic Exchange Service (DAAD) with funds from the German Federal Ministry of Education and Research (BMBF).

References

[1] Moulijn JA. Chemical process technology. 2nd ed. Chichester, West Sussex: John Wiley & Sons Inc; 2013.

[2] Kroschwitz JI, Kirk RE, Othmer DF, Seidel A (eds.). Kirk-Othmer encyclopedia of chemical technology. 5th ed. Hoboken, NJ: Wiley-Interscience; 2004.

[3] García Cortés C, Tzimas E, Peteves SD. Technologies for coal based hydrogen and electricity co-production power plants with CO2 capture. Luxembourg: Office for Official Publications of the European Communities; 2009.

[4] Andrews JW. Hydrogen production and carbon sequestration by steam methane reforming and fracking with carbon dioxide. International Journal of Hydrogen Energy 2020;45(16):9279–84. https://doi.org/10.1016/j.ijhydene.2020.01.231.

[5] van Selow ER, Cobden PD, Verbraeken PA, Hufton JR, van den Brink RW. Carbon Capture by Sorption-Enhanced Water−Gas Shift Reaction Process using Hydrotalcite-Based Material. Ind. Eng. Chem. Res. 2009;48(9):4184–93. https://doi.org/10.1021/ie801713a.

[6] Coenen K, Gallucci F, Pio G, Cobden P, van Dijk E, Hensen E et al. On the influence of steam on the CO2 chemisorption capacity of a hydrotalcite-based adsorbent for SEWGS applications. Chem Eng J 2017;314:554–69. https://doi.org/10.1016/j.cej.2016.12.013.

[7] Carboni M, Pio G, Mocellin P, Pilo F, Vianello C, Russo P et al. Experimental and numerical characterization of hydrogen jet fires. International Journal of Hydrogen Energy 2022;47(51):21883–96. https://doi.org/10.1016/j.ijhydene.2022.05.010.

[8] Molkov V, Saffers J-B. Hydrogen jet flames. International Journal of Hydrogen Energy 2013;38(19):8141–58. https://doi.org/10.1016/j.ijhydene.2012.08.106.

[9] Kim HY, Lee J, Kim NI. Effects of N 2 /CO 2 dilution on flame propagation velocities and quenching distances of oxy-methane premixed mixtures using an Annular-Stepwise-Diverging-Tube (ASDT). Math. Model. Nat. Phenom. 2018;13(6):55. https://doi.org/10.1051/mmnp/2018053.

[10] Zhou A, Li X-s, Ren X-d, Li X, Gu C-w. Evaluation of the performance and economy for a hybrid energy storage system using hydrogen and compressed carbon dioxide as the energy carrier. Energy Convers Manag 2022;264:115700. https://doi.org/10.1016/j.enconman.2022.115700.

[11] Allam R, Martin S, Forrest B, Fetvedt J, Lu X, Freed D et al. Demonstration of the Allam Cycle: An Update on the Development Status of a High Efficiency Supercritical Carbon Dioxide Power Process Employing Full Carbon Capture. Energy Procedia 2017;114:5948–66. https://doi.org/10.1016/j.egypro.2017.03.1731.

[12] Davis SG, Joshi AV, Wang H, Egolfopoulos F. An optimized kinetic model of H2/CO combustion. Proc Combust Inst 2005;30(1):1283–92. https://doi.org/10.1016/j.proci.2004.08.252.

[13] Kim YS, Jeon J, Song CH, Kim SJ. Improved prediction model for H2/CO combustion risk using a calculated non-adiabatic flame temperature model. Nucl Eng Technol 2020;52(12):2836–46. https://doi.org/10.1016/j.net.2020.07.040.

[14] Miao H, Lu L, Huang Z. Flammability limits of hydrogen-enriched natural gas. International Journal of Hydrogen Energy 2011;36(11):6937–47. https://doi.org/10.1016/j.ijhydene.2011.02.126.

[15] Salzano E, Pio G, Ricca A, Palma V. The effect of a hydrogen addition to the premixed flame structure of light alkanes. Fuel 2018;234:1064–70. https://doi.org/10.1016/j.fuel.2018.07.110.

[16] Eckart S, Prieler R, Hochenauer C, Krause H. Application and comparison of multiple machine learning techniques for the calculation of laminar burning velocity for hydrogen-methane mixtures. Therm Sci Eng Prog 2022;32:101306. https://doi.org/10.1016/j.tsep.2022.101306.

[17] Tan Y, Douglas MA, Thambimuthu KV. CO2 capture using oxygen enhanced combustion strategies for natural gas power plants. Fuel 2002;81(8):1007–16. https://doi.org/10.1016/S0016-2361(02)00014-5.

[18] Qian Y, Sun S, Ju D, Shan X, Lu X. Review of the state-of-the-art of biogas combustion mechanisms and applications in internal combustion engines. Renewable Sustainable Energy Rev 2017;69:50–8. https://doi.org/10.1016/j.rser.2016.11.059.

[19] Francisco Jr. RW, Costa M, Catapan RC, Oliveira AAM. Combustion of hydrogen rich gaseous fuels with low calorific value in a porous burner placed in a confined heated environment. Exp Therm Fluid Sci 2013;45:102–9. https://doi.org/10.1016/j.expthermflusci.2012.10.011.

[20] Pio G, Ricca A, Palma V, Salzano E. Experimental and numerical evaluation of low-temperature combustion of bio-syngas. International Journal of Hydrogen Energy 2020;45(1):1084–95. https://doi.org/10.1016/j.ijhydene.2019.10.207.

[21] Oliveira GP, Sbampato ME, Martins CA, Santos LR, Barreta LG, Boschi Gonçalves RF. Experimental laminar burning velocity of syngas from fixed-bed downdraft biomass gasifiers. Renew Energy 2020;153:1251–60. https://doi.org/10.1016/j.renene.2020.02.083.

[22] Djebaili N, Lisbet R, Paillard C, Dupré G. Comparison between the Ignition of H2-Air-CO2 and H2-Air-H2O Mixtures by a Hot Gas Jet. In: Brun R, Dumitrescu LZ, editors. Shock Waves Marseille II: Physico-Chemical Processes and Nonequilibrium Flow. Berlin, Heidelberg: Springer; 1995, p. 149–154.

[23] Paidi SK, Bhavaraju A, Akram M, Kumar S. Effect of N2/CO2 dilution on laminar burning velocity of H2–air mixtures at high temperatures. International Journal of Hydrogen Energy 2013;38(31):13812–21. https://doi.org/10.1016/j.ijhydene.2013.08.024.

[24] Eckart S, Pio G, Krause H, Salzano E. Chemical and thermal effects of trace components in hydrogen rich gases on combustion. Chemical Engineering Transactions 2022;90:361–6. https://doi.org/10.3303/CET2290061.

[25] Konnov AA, Dyakov IV. Experimental study of adiabatic cellular premixed flames of methane (ethane, propane) + oxygen + carbon dioxide mixtures. Combust Sci Technol 2007;179(4):747–65. https://doi.org/10.1080/00102200601057550.

[26] Jin W, Wang J, Yu S, Nie Y, Xie Y, Huang Z. Cellular instabilities of non-adiabatic laminar flat methane/hydrogen oxy-fuel flames highly diluted with CO2. Fuel 2015;143:38–46. https://doi.org/10.1016/j.fuel.2014.11.036.

[27] Yu JF, Yu R, Bai XS. Onset of cellular instability in adiabatic H2/O2/N2 premixed flames anchored to a flat-flame heat-flux burner. International Journal of Hydrogen Energy 2013;38(34):14866–78. https://doi.org/10.1016/j.ijhydene.2013.09.075.

[28] Pio G, Barba D, Palma V, Salzano E. A Numerical Study on the Effect of Temperature and Composition on the Flammability of Methane–Hydrogen Sulfide Mixtures. Combustion Science and Technology 2019;191(9):1541–57. https://doi.org/10.1080/00102202.2018.1564746.

[29] Goodwin DG, Speth RL, Moffat HK, Weber BW. Cantera: An object-oriented software toolkit for chemical kinetics, thermodynamics, and transport processes: Version 2.5.1. 2021.

[30] Pio G, Palma V, Salzano E. Comparison and Validation of Detailed Kinetic Models for the Oxidation of Light Alkenes. Ind. Eng. Chem. Res. 2018;57(21):7130–5. https://doi.org/10.1021/acs.iecr.8b01377.

[31] Damodara VD, Alphones A, Chen DH, Lou HH, Martin C, Li X. Flare performance modeling and set point determination using artificial neural networks. Int J Energy Environ Eng 2020;11(1):91–109. https://doi.org/10.1007/s40095-019-00314-3.

[32] Gao X, Yang S, Sun W. A global pathway selection algorithm for the reduction of detailed chemical kinetic mechanisms. Combust Flame 2016;167:238–47. https://doi.org/10.1016/j.combustflame.2016.02.007.

[33] Du Wang, Ji C, Wang S, Meng H, Wang Z, Yang J. Further understanding the premixed methane/hydrogen/air combustion by global reaction pathway analysis and sensitivity analysis. Fuel 2020;259:116190. https://doi.org/10.1016/j.fuel.2019.116190.

[34] Law CK, Egolfopoulos FN. A kinetic criterion of flammability limits: The C-H-O-inert system. Symp (Int.) Combust 1991;23(1):413–21. https://doi.org/10.1016/S0082-0784(06)80286-9.

[35] Kazakov A, Frenklach M. DRM reaction mechanism 1994.

[36] Battin-Leclerc F. Detailed chemical kinetic models for the low-temperature combustion of hydrocarbons with application to gasoline and diesel fuel surrogates. Prog Energy Combust Sci 2008;34(4):440–98. https://doi.org/10.1016/j.pecs.2007.10.002.

[37] Pio G, Dong X, Salzano E, Green WH. Automatically generated model for light alkene combustion. Combust Flame 2022;241:112080. https://doi.org/10.1016/j.combustflame.2022.112080.

[38] Konnov AA, Mohammad A, Kishore VR, Kim NI, Prathap C, Kumar S. A comprehensive review of measurements and data analysis of laminar burning velocities for various fuel+air mixtures. Prog Energy Combust Sci 2018;68:197–267.

[39] Smith GP, Bowman T, Frenklach M, Golden GM, Moriarty N, Eiteneer B et al. GRI-MECH 3.0 http://combustion.berkeley.edu/gri-mech/ 2000.

[40] Kee RJ, Coltrin ME, Glarborg P. Chemically reacting flow: Theory and practice. Hoboken, NJ: Wiley-Interscience; 2005.

[41] Li J, Zhao Z, Kazakov A, Dryer FL. An updated comprehensive kinetic model of hydrogen combustion. Int. J. Chem. Kinet. 2004;36(10):566–75. https://doi.org/10.1002/kin.20026.

[42] Konnov AA. Detailed reaction mechanism for small hydrocarbons combustion, Release 0.5. http://homepages.vub.ac.be/~akonnov/ 2000.

[43] Ó Conaire M, Curran HJ, Simmie JM, Pitz WJ, Westbrook CK. A comprehensive modeling study of hydrogen oxidation. Int. J. Chem. Kinet. 2004;36(11):603–22. https://doi.org/10.1002/kin.20036.

[44] Alekseev VA, Konnov AA. Data consistency of the burning velocity measurements using the heat flux method: Hydrogen flames. Combust Flame 2018;194:28–36. https://doi.org/10.1016/j.combustflame.2018.04.011.

[45] Pio G, Renda S, Palma V, Salzano E. Safety parameters for oxygen-enriched flames. J Loss Prev Process Ind 2020;65:104151. https://doi.org/10.1016/j.jlp.2020.104151.

[46] de Goey LPH, van Maaren A, Quax RM. Stabilization of adiabatic premixed laminar flames on a flat flame burner. Combust Sci Technol 1993;92(1-3):201–7.

[47] Botha JP, Spalding DB. The Laminar Flame Speed of Propane/Air Mixtures with Heat Extraction from the Flame. Proceedings of the Royal Society A: Mathematical, Physical and Engineering Sciences 1954;225(1160):71–96.

[48] van Maaren A, de Goey LPH. Laser doppler thermometry in flat flames. Combust Sci Technol 1994;99(1-3):105–18.

[49] Eckart S, Pizzuti L, Fritsche C, Krause H. Experimental study and proposed power correlation for laminar burning velocity of hydrogen-diluted methane with respect to pressure and temperature variation. International Journal of Hydrogen Energy 2022(47):6334–48. https://doi.org/10.1016/j.ijhydene.2021.11.243.

[50] de Goey LPH, Somers LMT, Bosch WMML, Mallens RMM. Modeling of the Small Scale Structure of Flat Burner-Stabilized Flames. Combust Sci Technol 1995;104(4-6):387–400. https://doi.org/10.1080/00102209508907729.

[51] Döntgen M, Eckart S, Fritsche C, Krause H, Heufer KA. Experimental and chemical kinetic modeling study of trimethoxy methane combustion. Proceedings of the Combustion Institute 2022. https://doi.org/10.1016/j.proci.2022.09.023.

[52] Alekseev VA, Naucler JD, Christensen M, Nilsson EJK, Volkov EN, de Goey LPH et al. Experimental uncertainties of the heat flux method for measuring burning velocities. Combust Sci Technol 2016;188(6):853–94. https://doi.org/10.1080/00102202.2015.1125348.

[53] Eckart S, Penke C, Voss S, Krause H. Laminar burning velocities of low calorific and hydrogen containing fuel blends. Energy Procedia 2017(120):149–56. https://doi.org/10.1016/j.egypro.2017.07.148.

[54] Shrestha KP, Eckart S, Elbaz AM, Giri BR, Fritsche C, Seidel L et al. A comprehensive kinetic model for dimethyl ether and dimethoxymethane oxidation and NOx interaction utilizing experimental laminar flame speed measurements at elevated pressure and temperature. Combust Flame 2020(218):57–74. https://doi.org/10.1016/j.combustflame.2020.04.016.

[55] Eckart S, Cai L, Fritsche C, vom Lehn F, Pitsch H, Krause H. Laminar burning velocities, CO and NOx emissions of premixed polyoxymethylene dimethyl ether flames. Fuel 2021(293).

[56] Eckart S, Fritsche C, Krasselt C, Krause H. Determining the laminar burning velocity of nitrogen diluted dimethoxymethane (OME1) using the heat-flux burner method: Numerical and experimental investigations. Int. J. Energy Res. 2020(45):2824–36.

[57] Rau F, Hartl S, Voss S, Still M, Hasse C, Trimis D. Laminar burning velocity measurements using the Heat Flux method and numerical predictions of iso-octane/ethanol blends for different preheat temperatures. Fuel 2015;140:10–6.

[58] Zhang F, Bonart H, Zirwes T, Habisreuther P, Bockhorn H, Zarzalis N. Direct Numerical Simulation of Chemically Reacting Flows with the Public Domain Code OpenFOAM. In: Kröner D, Resch M, Nagel WE, editors. High Performance Computing in Science and Engineering ‘14: Transactions of the High Performance Computing Center, Stuttgart (HLRS) 2014. Cham: Springer; 2015, p. 221–236.

[59] Zirwes T, Zhang F, Denev JA, Habisreuther P, Bockhorn H. Automated Code Generation for Maximizing Performance of Detailed Chemistry Calculations in OpenFOAM. In: Nagel WE, Kröner D, Resch M, editors. High Performance Computing in Science and Engineering ‘ 17: Transactions of the High Performance Computing Center, Stuttgart (HLRS) 2017. Cham: Springer; 2018, p. 189–204.

[60] Zirwes T, Zhang F, Habisreuther P, Hansinger M, Bockhorn H, Pfitzner M et al. Quasi-DNS Dataset of a Piloted Flame with Inhomogeneous Inlet Conditions. Flow Turbulence Combust 2020;104(4):997–1027. https://doi.org/10.1007/s10494-019-00081-5.

[61] OpenFOAM. The open surce CFD toolbox.

[62] Wen X, Zirwes T, Scholtissek A, Böttler H, Zhang F, Bockhorn H et al. Flame structure analysis and composition space modeling of thermodiffusively unstable premixed hydrogen flames — Part I: Atmospheric pressure. Combust Flame 2022;238:111815. https://doi.org/10.1016/j.combustflame.2021.111815.

[63] Zirwes, T., Zhang, F., Denev, J.A., Habisreuther, P., Bockhorn, H., Trimis, D. (2019). Improved Vectorization for Efficient Chemistry Computations in OpenFOAM for Large Scale Combustion Simulations. In: Nagel, W., Kröner, D., Resch, M. (eds) High Performance Computing in Science and Engineering ‘ 18. Springer, Cham. https://doi.org/10.1007/978-3-030-13325-2_1

[64] Zirwes T, Zhang F, Häber T, Bockhorn H. Ignition of combustible mixtures by hot particles at varying relative speeds. Combustion Science and Technology 2019;191(1):178–95. https://doi.org/10.1080/00102202.2018.1435530.

[65] Zirwes T, Häber T, Zhang F, Kosaka H, Dreizler A, Steinhausen M et al. Numerical Study of Quenching Distances for Side-Wall Quenching Using Detailed Diffusion and Chemistry. Flow Turbulence Combust 2020. https://doi.org/10.1007/s10494-020-00215-0.

[66] Berger L, Kleinheinz K, Attili A, Pitsch H. Characteristic patterns of thermodiffusively unstable premixed lean hydrogen flames. Proc Combust Inst 2019;37(2):1879–86. https://doi.org/10.1016/j.proci.2018.06.072.

[67] Wen X, Zirwes T, Scholtissek A, Böttler H, Zhang F, Bockhorn H et al. Flame structure analysis and composition space modeling of thermodiffusively unstable premixed hydrogen flames — Part

II: Elevated pressure. Combust Flame 2021:111808. https://doi.org/10.1016/j.combustflame.2021.111808.